Paper 4

Neutral atmosphere temperature trends and variability at 90 km, 70°N, 19°E, 2003–2014

Holmen, S. E., C. M. Hall and M. Tsutsumi

Published in Atmospheric Chemistry and Physics, 16, 7853-7866, doi: 10.5194/acp-16-7853-2016, 2016.

Atmos. Chem. Phys., 16, 7853–7866, 2016
www.atmos-chem-phys.net/16/7853/2016/
doi:10.5194/acp-16-7853-2016

Atmospheric Chemistry and Physics Open Access EGU

Neutral atmosphere temperature trends and variability at 90 km, 70° N, 19° E, 2003–2014

Silje Eriksen Holmen[1,2,3], **Chris M. Hall**[2], **and Masaki Tsutsumi**[4,5]

[1]The University Centre in Svalbard, Longyearbyen, Norway
[2]Tromsø Geophysical Observatory, UiT – The Arctic University of Norway, Tromsø, Norway
[3]Birkeland Centre for Space Science, Bergen, Norway
[4]National Institute of Polar Research, Tokyo, Japan
[5]The Graduate University for Advanced Studies (SOKENDAI), Department of Polar Science, Hayama, Japan

Correspondence to: Silje Eriksen Holmen (siljeh@unis.no)

Received: 28 April 2015 – Published in Atmos. Chem. Phys. Discuss.: 5 June 2015
Revised: 11 May 2016 – Accepted: 6 June 2016 – Published: 27 June 2016

Abstract. Neutral temperatures at 90 km height above Tromsø, Norway, have been determined using ambipolar diffusion coefficients calculated from meteor echo fading times using the Nippon/Norway Tromsø Meteor Radar (NTMR). Daily temperature averages have been calculated from November 2003 to October 2014 and calibrated against temperature measurements from the Microwave Limb Sounder (MLS) on board Aura. Large-scale periodic oscillations ranging from ∼9 days to a year were found in the data using Lomb–Scargle periodogram analysis, and these components were used to seasonally detrend the daily temperature values before assessing trends. Harmonic oscillations found are associated with the large-scale circulation in the middle atmosphere together with planetary and gravity wave activity. The overall temperature change from 2003 to 2014 is $-2.2\,\mathrm{K} \pm 1.0\,\mathrm{K\,decade^{-1}}$, while in summer (May–June–July) and winter (November–December–January) the change is $-0.3\,\mathrm{K} \pm 3.1\,\mathrm{K\,decade^{-1}}$ and $-11.6\,\mathrm{K} \pm 4.1\,\mathrm{K\,decade^{-1}}$, respectively. The temperature record is at this point too short for incorporating a response to solar variability in the trend. How well suited a meteor radar is for estimating neutral temperatures at 90 km using meteor trail echoes is discussed, and physical explanations behind a cooling trend are proposed.

1 Introduction

Temperature changes in the mesosphere and lower thermosphere (MLT) region due to both natural and anthropogenic variations cannot be assessed without understanding the dynamical, radiative and chemical couplings between the different atmospheric layers. Processes responsible for heating and cooling in the MLT region are many. Absorption of UV by O_3 and O_2 causes heating, while CO_2 causes strong radiative cooling. Planetary waves (PWs) and gravity waves (GWs) break and deposit heat and momentum into the middle atmosphere and influence the mesospheric residual circulation, which is the summer-to-winter circulation in the mesosphere. Also, heat is transported through advection and adiabatic processes.

For decades, it has been generally accepted that increased anthropogenic emissions of greenhouse gases are responsible for warming of the lower atmosphere (e.g. Manabe and Wetherald, 1975) and that these emissions are causing the mesosphere and thermosphere to cool (Akmaev and Fomichev, 2000; Roble and Dickinson, 1989). Akmaev and Fomichev (1998) report, using a middle atmospheric model, that if CO_2 concentrations are doubled, temperatures will decrease by about 14 K at the stratopause, by about 10 K in the upper mesosphere and by 40–50 K in the thermosphere. Newer and more sophisticated models include important radiative and dynamical processes as well as interactive chemistries. Some model results indicate a cooling rate near the mesopause lower than predicted by Akmaev and Fomichev (1998), while others maintain the negative signal

(French and Klekociuk, 2011; Beig, 2011). The thermal response in this region is strongly influenced by changes in dynamics, and some dynamical processes contribute to a warming which counteracts the cooling expected from greenhouse gas emissions (Schmidt et al., 2006).

Even though the increasing concentration of greenhouse gases is generally accepted to be the main driver, other drivers of long-term changes and temperature trends also exist, namely stratospheric ozone depletion, long-term changes of solar and geomagnetic activity, secular changes of the Earth's magnetic field, long-term changes of atmospheric circulation and mesospheric water vapour concentration (Laštovička et al., 2012). Dynamics may influence temperatures in the MLT region on timescales of days to months, and investigations of the influence of this variability on averages used for temperature trend assessments are important. The complexity of temperature trends in the MLT region and their causes act as motivation for studying these matters further.

In this paper, we investigate trend and variability of temperatures obtained from the Nippon/Norway Tromsø Meteor Radar (NTMR), and we also look at summer and winter seasons separately. In Sect. 2, specifications of the NTMR radar are given, and the theory behind the retrieval of temperatures using ambipolar diffusion coefficients from meteor trail echoes is explained. In Sect. 3, the method behind the calibration of NTMR temperatures against Aura MLS temperatures is explained. Section 4 treats trend analysis and analysis of variability and long-period oscillations in temperatures. The theory and underlying assumptions for the method used for determining neutral temperatures from meteor trail echoes, thus how well suited a meteor radar is for estimating such temperatures is discussed in Sect. 5. Also, physical explanations behind changes in temperature and observed temperature variability are discussed, as well as comparison with other reports on trends.

2 Instrumentation and data

The NTMR is located at Ramfjordmoen near Tromsø, at 69.58° N, 19.22° E. It is operated 24 h per day, all year round. Measurements are available for more than 90 % of all days since the radar was first operative in November 2003. The meteor radar consists of one transmitter antenna and five receivers and is operating at 30.25 MHz. It detects echoes from ionised trails from meteors, which appear when meteors enter and interact with the Earth's neutral atmosphere in the MLT region. The ionised atoms from the meteors are thermalised, and the resulting trails expand in the radial direction mainly due to ambipolar diffusion, which is diffusion in plasma due to interaction with the electric field. Underdense meteors, which are the ones used in this study, have a plasma frequency that is lower than the frequency of the radar, which makes it possible for the radio wave from the radar to penetrate into the meteor trail and be scattered by each electron.

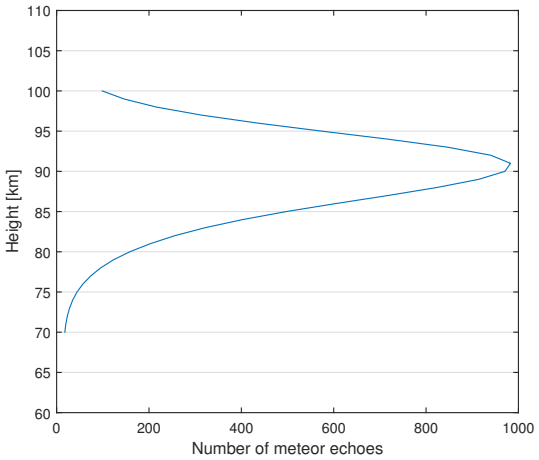

Figure 1. Vertical distribution of the occurrence of meteor echoes over Tromsø, averaged over height between 2003 and 2014. The peak occurrence height is just over 90 km altitude.

Echoes are detected from a region within a radius of approximately 100 km (horizontal space). The radar typically detects around 10 000 echoes per day, of which around 200–600 echoes are detected per hour at the peak occurrence height of 90 km. Figure 1 shows the vertical distribution of meteor echoes as a function of height, averaged over the time period 2003–2014. The number of echoes detected per day allows for a 30 min resolution of temperature values. The intraday periodicity in meteor detections by the NTMR radar is less pronounced than that of lower-latitude stations and we do not anticipate tidally induced bias regarding echo rates at specific tidal phases for daily averages. The height resolution and the range resolution are both 1 km, when looking at altitudes around the peak occurrence height. From the decay time of the radar signal we can derive ambipolar diffusion coefficients, D_a:

$$D_a = \frac{\lambda^2}{16\pi^2\tau}, \quad (1)$$

where λ is the radar wavelength and τ is the radar echo decay time. It has been shown that this coefficient also can be expressed in terms of atmospheric temperature and pressure:

$$D_a = 6.39 \times 10^{-2} K_0 \frac{T^2}{p}, \quad (2)$$

where p is pressure, T is temperature and K_0 is the zero-field reduced mobility factor of the ions in the trail. In this study we used the value for K_0 of $2.4 \times 10^{-4}\,\mathrm{m^2\,s^{-1}\,V^{-1}}$, in accordance e.g. with Holdsworth et al. (2006). Pressure values were derived from atmospheric densities obtained from falling sphere measurements appropriate for 70° N, combining those of Lübken and von Zahn (1991) and Lübken (1999), previously used by e.g. Holdsworth (2006) and Dyrland et al. (2010). These densities do not take into account long-term solar cycle variations.

The NTMR radar is essentially identical to the Nippon/Norway Svalbard Meteor Radar (NSMR) located in Advent Valley on Spitsbergen at 78.33° N, 16.00° E. Further explanation of the radar and explanation of theories can be found in e.g. Hall et al. (2002), Hall et al. (2012), Cervera and Reid (2000) and McKinley (1961).

Calibration of temperatures derived from meteor echoes with an independent, coinciding temperature series is necessary, according to previous studies (e.g. Hocking, 1999). Temperatures from the NSMR radar have been derived most recently by Dyrland et al. (2010), employing a new calibration approach for the meteor radar temperatures, wherein temperature measurements from the Microwave Limb Sounder (MLS) on the Aura satellite were used instead of the previously used rotational hydroxyl and potassium lidar temperatures from ground-based optical instruments (Hall et al., 2006). Neither ground-based optical observations nor lidar soundings are available for the time period of interest or the location of the NTMR. In this study we therefore employ the same approach as Dyrland et al. (2010), using Aura MLS temperatures to calibrate the NTMR temperatures.

NASA's EOS Aura satellite was launched 15 July 2004 and gives daily global coverage (between 82° S and 82° N) with about 14.5 orbits per day. The MLS instrument is one of four instruments on Aura and samples viewing forward along the spacecraft's flight direction, scanning its view from the ground to $\sim$ 90 km every $\sim$ 25 s, making measurements of atmospheric temperature, among others (NASA Jet Propulsion Laboratory, 2015).

Because of a general cooling of most of the stratosphere and mesosphere the last decades due to e.g. altered concentrations of CO_2 and O_3, the atmosphere has been shrinking, leading to a lowering of pressure surfaces at various altitudes. It is important to distinguish between trends on fixed pressure altitudes and fixed geometric altitudes, since trends on geometric altitudes include the effect of a shrinking atmosphere (Lübken et al., 2013). In this study, we have obtained Aura MLS temperature data (version 3.3) for latitude 69.7° N ± 5.0° and longitude 19.0° E ± 10.0° at 90 km geometric altitude.

3 Calibration of NTMR temperatures

Figure 2 shows daily NTMR temperatures from November 2003 to October 2014, derived from Eqs. (1) and (2), plotted together with Aura MLS temperatures. Standard error of the mean is omitted in the plot for better legibility, but typical standard error for daily temperatures is 0.2–0.6 K, highest in winter. The Aura satellite overpasses Tromsø at 01:00–03:00 and 10:00–12:00 UTC, which means that the Aura daily averages are representative for these time windows. It was therefore necessary to investigate any bias arising from Aura not measuring throughout the whole day. A way to do this is to

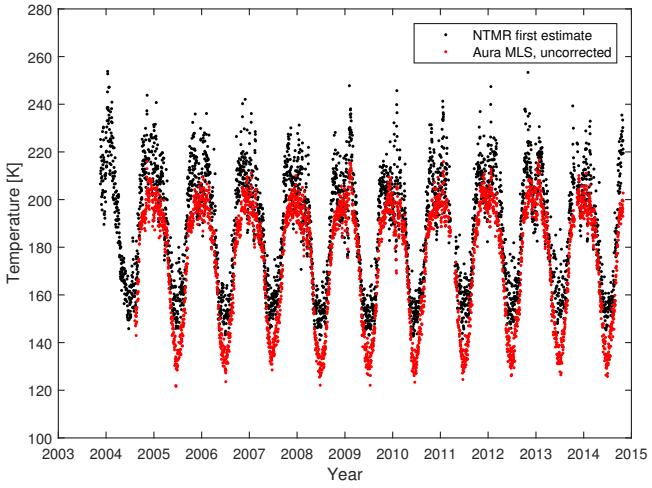

Figure 2. Daily values of NTMR temperatures derived from Eqs. (1) and (2) before correction for high D_a, plotted together with Aura MLS temperatures before applying any corrections.

assume that Aura temperatures and NTMR temperatures follow the same diurnal variation and thus investigate the diurnal variation of NTMR temperatures. This was done by superposing all NTMR temperatures by time of day, obtaining 48 values for each day, since the radar allows for a 30 min resolution.

There is an ongoing investigation into the possibility that D_a derived by NTMR can be affected by modified electron mobility during auroral particle precipitation. According to Rees et al. (1972), neutral temperatures in the auroral zone show a positive correlation with geomagnetic activity. It is therefore a possibility that apparent D_a enhancements during strong auroral events do not necessarily depict neutral temperature increase. This matter requires further attention.

Plotting hourly D_a values shows clear evening enhancements, especially during winter (not shown here). Investigation of possible unrealistic D_a enhancements was carried out by calculating standard errors of estimated hourly D_a values:

$$\mathrm{se} = \frac{\sigma}{\sqrt{\mathrm{ne}}}, \tag{3}$$

where σ is standard deviation and ne is the number of echoes detected by the radar. By examining and testing different rejection criteria, we arrived at a threshold of 7 % in standard error of hourly D_a values for identifying unrealistic enhancements. This rejection criterion led to that 5.4 % of the D_a values were rejected. NTMR temperatures after application of the D_a rejection procedure will hereafter be referred to as D_a-rejected NTMR temperatures.

Figure 3 shows monthly averages of the superposed values of D_a-rejected NTMR temperatures as a function of time of day for days coinciding with Aura measurements. It is evident from the figure that the lowest temperatures are in general achieved in the forenoon, which coincides with one of

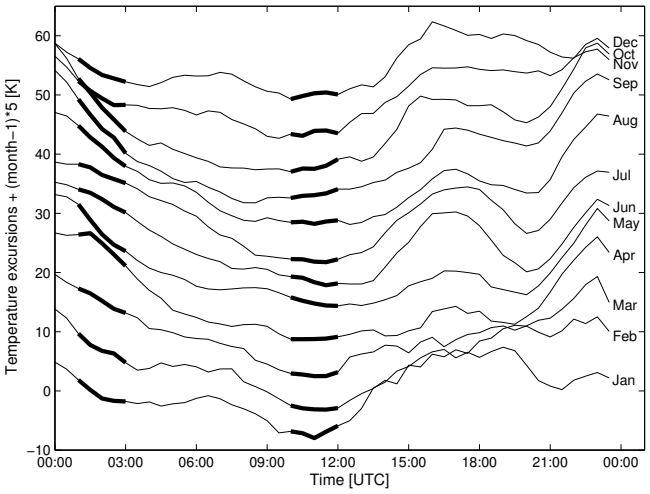

Figure 3. Monthly averages of diurnal temperature variation derived from NTMR after correction for high D_a at 90 km altitude. For clarity, time series are displaced by 5 K per month subsequent to January. The time of day corresponding to when Aura makes measurements over Tromsø (01:00–03:00 and 10:00–12:00 UTC) is highlighted.

the periods per day when Aura MLS makes measurements over Tromsø.

Subtracting monthly averages of the 00:00–24:00 UTC temperatures from the 01:00–03:00 and 10:00–12:00 UTC temperatures gave the estimated biases in Aura daily means due to only sampling during some hours of the day and are given in Table 1. By judging by the measurement windows, Aura underestimates the daily mean (00:00–24:00 UTC) more during winter than during spring and summer. Note the higher standard deviations in spring and summer compared with winter.

The initially obtained Aura temperatures were corrected by adding the biases from Table 1 in order to arrive at daily mean temperatures that were representative for the entire day. Also, the Aura temperatures were corrected for "cold bias". French and Mulligan (2010) report that Aura MLS temperatures exhibit a 10 K cold bias compared with OH*(6–2) nightly temperatures at Davis Station, Antarctica. A newer study by García-Comas et al. (2014) shows that Aura MLS exhibits a bias compared with several satellite instruments which varies with season. According to their findings, a 10 K correction for cold bias was applied to the Aura summer and winter temperatures (June–August, December–February), while a 5 K correction was applied to autumn and spring temperatures (September–November, March–May). The corrected Aura temperatures will hereafter be referred to as local time and cold bias-corrected Aura MLS temperatures.

Local time and cold bias-corrected Aura temperatures were plotted against D_a-rejected NTMR temperatures, and the linear fit ($R^2 = 0.83$) is described by:

$$T_{\mathrm{NTMR}} = 0.84\, T_{\mathrm{Aura}} + 32, \tag{4}$$

where T_{NTMR} is D_a-rejected temperature obtained from NTMR, and T_{Aura} is local time and cold bias-corrected temperature from Aura MLS. Inverting Eq. (4) enabled us to estimate NTMR temperatures calibrated with respect to Aura MLS temperatures. NTMR temperatures were now corrected for days of measurements coinciding with Aura measurements and are hereafter referred to as MLS-calibrated NTMR temperatures. For calibration of NTMR temperatures from November 2003 to August 2004 (before the beginning of the Aura MLS dataset), D_a-rejected NTMR temperatures were used as input to the inverted equation to arrive at calibrated NTMR temperatures.

To estimate the calibration uncertainty, all local time and cold bias-corrected Aura temperatures were subtracted from the MLS-calibrated NTMR temperatures, and the differences were plotted in a histogram with 5 K bins (not shown here). A Gaussian was fitted to the distribution. The standard deviation of the Gaussian was 11.9 K, which is considered to be the overall uncertainty of the calibration. Finally, Fig. 4 shows the MLS-calibrated NTMR temperatures with uncertainties plotted together with Aura MLS temperatures, corrected for cold and time-of-day measurement bias.

4 Results

Weatherhead et al. (1998) discuss the effects of autocorrelation and variability on trend estimation and emphasise that changes in environmental variables are often modelled as being a linear change, even though there may be a high degree of periodic variation within the data in addition to the linear trend. A linear trend model assumes that measurements of the variable of interest at time t can be expressed as follows:

$$Y_t = \mu + S_t + \omega L_t + N_t, \tag{5}$$

where μ is a constant term, S_t is a seasonal component, L_t is the linear trend function, ω is the magnitude of the trend and N_t is noise. N_t may be autocorrelated and the result of various natural factors, which give rise to somewhat smoothly varying changes in N_t over time. Such natural factors may not always be known or measurable.

Taking this into account, variability of the data was explored before assessing the linear trend of the temperature data. In Sect. 4.1, a Lomb–Scargle periodogram analysis is conducted, and periodic components in the data are identified before assessing the trend, while in Sect. 4.2 solar cycle dependence is briefly explored, even though the temperature record is too short for this to be incorporated in the trend analysis.

Table 1. Bias/overestimate expected from Aura monthly averages due to Aura MLS only measuring between 01:00 and 03:00 UTC and between 10:00 and 12:00 UTC.

Month	Jan	Feb	Mar	Apr	May	Jun	Jul	Aug	Sep	Oct	Nov	Dec
Aura bias (K)	−6.3	−6.5	−3.3	−0.08	−0.5	−0.6	−1.4	−1.3	−2.7	−3.5	−3.9	−4.6
σ (K)	3.2	4.7	6.0	8.1	6.6	7.1	7.5	6.7	6.0	5.3	2.6	1.8

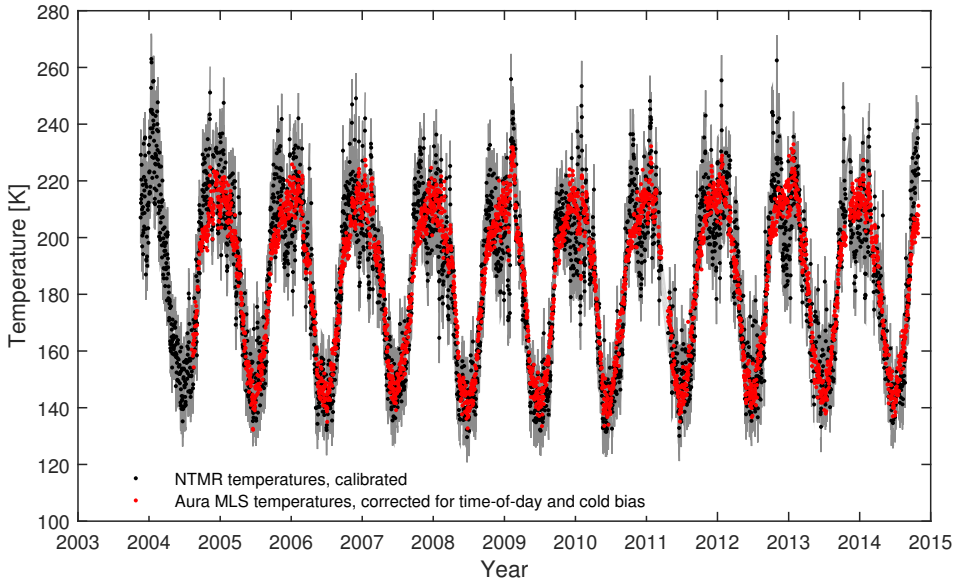

Figure 4. Daily values of MLS-calibrated NTMR temperatures plotted together with Aura MLS temperatures corrected for cold and time-of-day bias. The overall calibration uncertainty is indicated by the grey shading.

4.1 Estimation of periodic variability and trend

To identify periodic variability, a Lomb–Scargle (LS) periodogram analysis was applied to the MLS-corrected NTMR temperatures (Press and Rybicki, 1989). LS analysis is a modified discrete Fourier transform algorithm suitable for unevenly spaced data. Figure 5 (upper panel) shows the LS periodogram, identifying a particularly strong annual (A) component, but also a semi-annual (A/2) and two sub-annual peaks (A/3 and A/4), significant at the 99 % level.

Following the procedure of Niciejewski and Killeen (1995), the daily temperatures were fit to the following approximation:

$$T_{\mathrm{NTMR}}(t) = T_0 + \sum_i \left(d_i \sin \frac{2\pi}{p_i} t + e_i \cos \frac{2\pi}{p_i} t \right) + Lt, \quad (6)$$

where $T_{\mathrm{NTMR}}(t)$ is observed daily temperature, T_0 is the average temperature, i is the number of harmonic components found in the LS analysis, d_i and e_i are the amplitudes of the ith harmonic component, p_i is the period of the ith harmonic component and t is the day number. L represents the trend. The average temperature over the 11-year period, T_0, was found to be 189.4 ± 0.6 K.

It has been shown that the confidence levels in the periodogram are only strictly valid for the peak with the highest spectral power (Scargle, 1982). Thus, there may be peaks significant at the 95 % level even though they are not noticeable in the periodogram, due to their variance being overestimated by the presence of the larger peaks. Therefore, after fitting the primary periodic components with significance better than the 99 % level to the NTMR temperatures using Eq. (6), LS analysis was repeated on the temperature residuals to check for additional significant periodic components in the data. Horne and Baliunas (1986) point out that the periodogram power needs to be normalised by the total variance of the data in order to obtain spectral peaks with correct magnitude. The variance of the data was therefore adjusted to maintain the correct probability distribution of the periodogram. Figure 5 (lower panel) shows spectral power of harmonics found at better than 95 % significance level of residuals obtained after fitting the sinusoids of the four largest peaks. The apparently significant peaks located near 91, 121, 184 and 363 days, even though these harmonics have been filtered out at this stage, are due to spectral leakage, which means that for a sinusoidal signal at a given frequency, ω_0, the power in the periodogram not only appears at ω_0, but also leaks to other nearby frequencies (Scargle, 1982). All periodic components

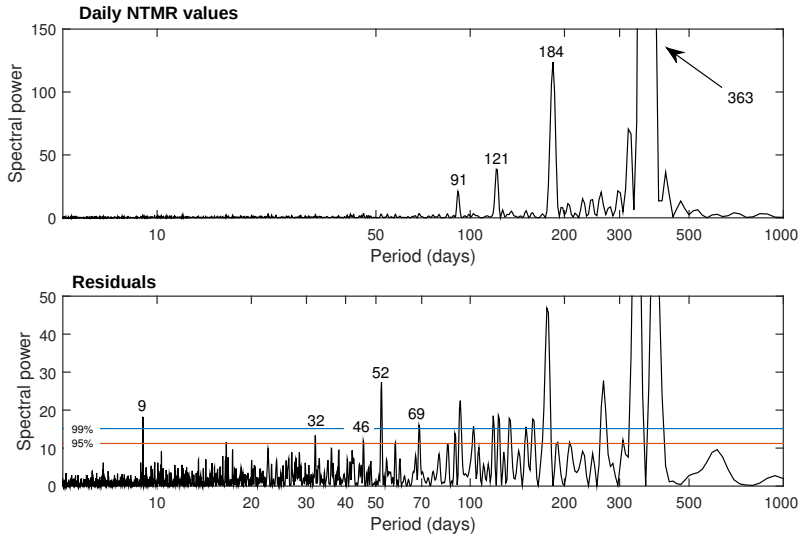

Figure 5. Upper panel: Lomb–Scargle periodogram for daily NTMR temperatures from 2003 to 2014. The y axis has been truncated for clarity. Lower panel: periodogram for residuals after fitting sinusoids for the four largest peaks from the upper panel. Peaks significant at better than 95 % are marked with numbers corresponding to period.

Table 2. Periodic components found in data using Lomb–Scargle periodogram analysis. All components were identified as better than the 99 % significance level, except for the 32-day harmonic, which was significant at the 95 % level. Amplitudes are given with 95 % confidence bounds.

Periodic component (days)	Amplitude (K)
363	21.5 ± 0.4
184	6.5 ± 0.4
121	3.8 ± 0.4
91	2.9 ± 0.4
69	1.2 ± 0.4
52	1.5 ± 0.4
46	1.1 ± 0.4
32	0.9 ± 0.4
9.0	1.0 ± 0.4

found at better than 95 % significance and their amplitudes are listed in Table 2.

The trend was estimated from the approximation in Eq. (6) to be $-2.2\,\mathrm{K} \pm 1.0\,\mathrm{K\,decade^{-1}}$. From Tiao et al. (1990), this trend can be considered significantly non-zero at the 5 % level, since the uncertainty ($2\sigma = 2.0\,\mathrm{K\,decade^{-1}}$) is less than the trend itself. We estimated the number of years for which a trend can be detectable, following the formulation of Weatherhead et al. (1998):

$$n^* \approx \left(\frac{3.3\sigma_N}{|\omega_0|} \sqrt{\frac{1+\varphi}{1-\varphi}} \right)^{2/3}, \quad (7)$$

where n^* is the number of years required, ω_0 is the magnitude of the trend per year, σ_N is the standard deviation of noise N and φ is the autocorrelation function of the noise at lag 1. The value 3.3 corresponds to a 90 % probability that the trend is detectable after n^* years. Solving Eq. (7) reveals that the minimum number of years required for detecting a decadal trend of -2.2 K is about 17 years.

The resulting composite of the least-squares fit is shown in Fig. 6, together with the MLS-corrected NTMR temperatures. We see that the smooth curve represents the periodicity in the data to a good extent, but there is still variability not accounted for. Temperature residuals obtained after subtracting the MLS-calibrated NTMR temperatures from the fit in Fig. 6 are henceforth referred to as fit residuals.

In addition to the harmonics listed in Table 2, we found a harmonic of $\sim$615 days (see Fig. 5, lower panel), which was not statistically significant. We also found a $\sim$17-day oscillation, significant at the 95 % level (see Fig. 5, lower panel), but the amplitude of this component was found to be close to 0 K. The 615-day and 17-day periodic components were therefore not incorporated in the composite fit.

In Fig. 7, all individual years are superposed by day of year. This was done to better visualise the variability of an average year. In addition to the broad maximum in temperatures during winter and the narrower minimum during summer, we see minor enhancements just after the spring equinox (day of year $\sim$100) and summer solstice (day of year $\sim$210) and also a local minimum in early winter. Explanations for the variability will be discussed in Sect. 5.1.

In addition to the average temperature change, we also treated summer and winter seasons separately. First, monthly averages of the temperature residuals were calculated and

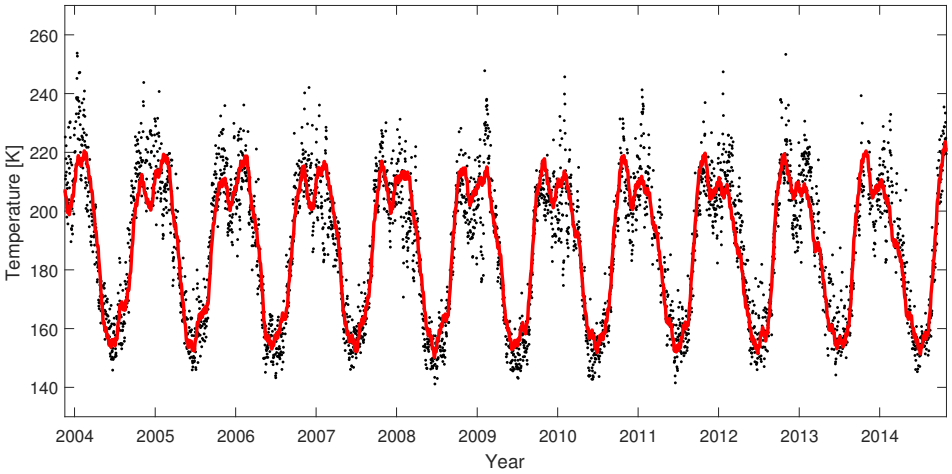

Figure 6. MLS-corrected NTMR daily temperatures (black dots) and the least-squares fit of the average, trend and periodic components (red curve).

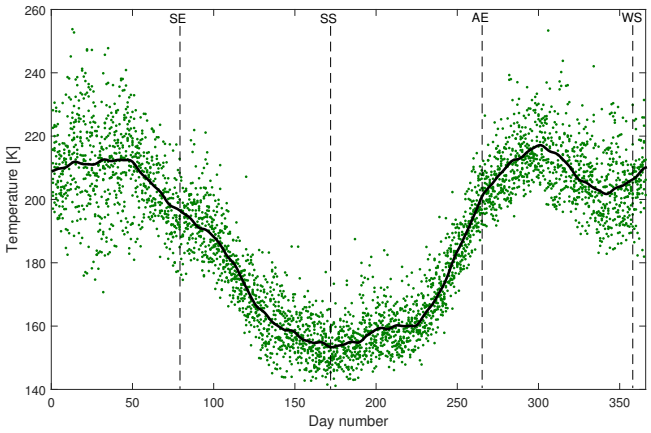

Figure 7. Superposed-epoch analysis of daily MLS-corrected NTMR temperatures. The smooth, black line is the composite fit of all periodic components listed in Table 2. Spring and autumn equinoxes and winter and summer solstice are marked SE, AE, WS and SS, respectively.

trends for each month were investigated. Figure 8 shows the result. Then, averages of November, December and January and of May, June and July were made. As opposed to the meteorological seasons as experienced in the troposphere, we have chosen to define "winter" and "summer" as the three months centred on the respective solstices. However, since the meteorological winter and summer are defined differently, we will refer to these trends as NDJ and MJJ trends. The linear NDJ trend is $-11.6\,\mathrm{K} \pm 4.1\,\mathrm{K\,decade}^{-1}$, and the MJJ trend is $-0.3\ \mathrm{K} \pm 3.1\,\mathrm{K\,decade}^{-1}$. Solving Eq. (7) for NDJ and MJJ trends reveals a minimum length for trend detection of 10.8 and 63 years, respectively.

The trend analysis was also performed without carrying out the D_a rejection procedure explained in Sect. 3. Final results of the trend analysis, both when excluding and including rejection of D_a values due to hypothetical anomalous electrodynamic processes, do not differ significantly. It is reasonable to believe that strong geomagnetic conditions can affect derived temperatures on a short timescale. However, due to the considerable quantity of data employed in this study, it is inconceivable that this effect will change the conclusions regarding trends, as our results also show.

4.2 Exploration of solar flux dependence

Our dataset covers 11 years of meteor radar temperatures and thus it is shorter than the corresponding solar cycle (which was somewhat longer than the average 11 years). Even though it is premature to apply solar cycle analysis to a time series this short, we will briefly explore and present our temperature data together with solar variability. In this study we use the F10.7 cm flux as a proxy for solar activity, which is the most commonly used index in middle/upper atmospheric temperature trend studies (e.g. Laštovicka et al., 2008; Hall et al., 2012).

Figure 9 shows yearly values of F10.7 cm plotted against yearly averaged fit residual temperatures. For clarity, black bullets corresponding to years are connected with lines, making it easier to see the progression from high solar flux to solar minimum and back to solar maximum. We see that, to some extent, there is a conjunction between low solar flux values and negative temperature fit residuals. For the years 2006–2010, which were years of solar minimum, fit residuals were on average negative. For the years 2005 and 2011, which were years in between solar maximum and minimum, fit residuals were close to zero. However, for years with higher F10.7 values the tendency of increasing fit residuals is less distinct. Ogawa et al. (2014) find a non-linear relationship between upper-atmospheric temperatures and solar activity using EISCAT UHF (ultra-high frequency) radar ob-

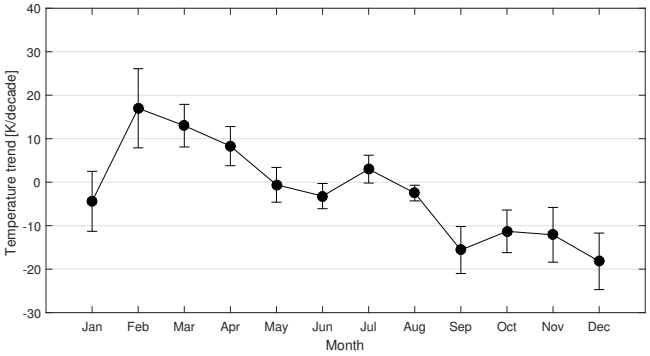

Figure 8. Monthly temperature trends at 90 km altitude over Tromsø. Standard deviations are given as error bars.

servations from 200 to 450 km altitude over Tromsø, even though it must be noted that the altitude range they look at differs from ours.

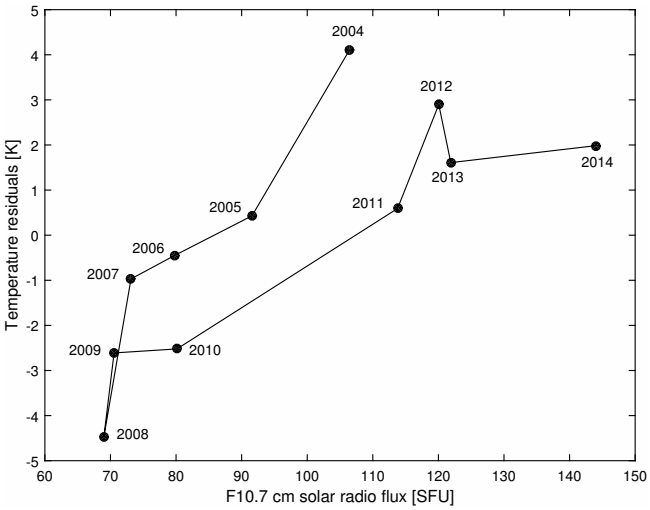

Figure 9. Yearly values of F10.7 cm solar radio flux plotted against yearly averaged temperature fit residuals. Year 2003 is left out of the figure due to the data coverage (only data for November and December).

5 Discussion

Statistically significant periodic components found in the temperature data are annual (A) and semi-annual (A/2) oscillations, and 121- (A/3), 91- (A/4), 69- (A/5), 52- (A/7), 46- (A/8), 32- and 9-day oscillations. Temperature change from 2003 to 2014 is $-2.2\,\mathrm{K} \pm 1.0\,\mathrm{K\,decade^{-1}}$, and MJJ and NDJ trends are $-0.3\,\mathrm{K} \pm 3.1$ and $-11.6\,\mathrm{K} \pm 4.1\,\mathrm{K\,decade^{-1}}$, respectively. Explanations for the periodic variability will be proposed in Sect. 5.1. In Sect. 5.2, physical explanations for the temperature change will be explored, and our results will be compared with other reports on mesospheric trends at high and midlatitudes. Trends will be discussed in terms of the method used for deriving temperatures in Sect. 5.3.

5.1 Mechanisms for the observed variability and harmonics

The A, A/2, A/3, A/4, A/5, A/7 and A/8 components are also found for OH* temperatures over other mid- and high-latitude sites (e.g. Espy and Stegman, 2002; Bittner et al., 2000; French and Burns, 2004). In addition to these components, A/6 and A/9 sub-annual harmonics, as well as other shorter-period components, have been identified in other datasets (e.g. Bittner et al., 2000; French and Burns, 2004).

Espy and Stegman (2002) attribute the asymmetry with the broad winter maximum and the narrow summer minimum to the A/2 harmonic, and the temperature enhancements during the equinoxes to the A/3 and A/4 harmonics.

French and Burns (2004) identify the visible variations of the 52-day (A/7) component in their data from Davis, Antarctica, and find this component's phase to be "locked" to the day of year, indicating a seasonal dependence. Espy and Stegman (2002) only find this component as a result of LS analysis of their superposed-epoch data, also indicating that the phase is locked to the day of year. French and Burns (2002) and Bittner et al. (2000) find in general strong differences from year to year in the significant oscillations observed. We have not carried out analysis of the year-to-year variation in oscillations observed, but considering, e.g. the uneven occurrences of SSWs (sudden stratospheric warnings), we have no reason to conclude otherwise regarding our data.

The $\sim$9-day oscillation we find in our data can most likely be designated to travelling planetary waves, which have typical periods of 1–3 weeks, with 8–10 days as a prominent period (Salby, 1981a, b).

The $\sim$615 day periodic component (not statistically significant) may at first glance seem to be somehow related to the quasi-biennial oscillation (QBO), which is a system where zonal winds in the lower equatorial stratosphere alternate between westward (easterly) and eastward (westerly) with a mean period of 28–29 months. Also other studies find a $\sim$2 year periodic component in their temperature data, attributed to a QBO effect (Espy and Stegman, 2002; Bittner et al., 2000; French and Burns, 2004 – the two latter give statistically inconclusive results). However, our $\sim$615 day component is quite far from the mean period of the QBO. That, in addition to it not being significant, makes it difficult to interpret.

The higher temperature variability during winter compared with summer, visible in Fig. 7, is also found in other datasets at mid- and high latitudes (e.g. Espy and Stegman, 2002; Bittner et al., 2000). This feature and the observations of local temperature enhancement around day 200 as well as the reduction of the strong, negative seasonal gradient just after the spring equinox can be explained by the state of the

background wind system in the middle atmosphere and the corresponding propagation of planetary and gravity waves. Enhanced GW and PW flux and momentum into the mesosphere lead to enhanced turbulent diffusion, which can result in increased temperatures. PWs can only propagate westward and against the zonal flow, so easterly winds in the middle atmosphere during summer are blocking vertical propagation of long-period PWs into the MLT region. In contrast, during winter stratospheric zonal winds are westerly, favouring PW propagation. The presence of upward-propagating PWs during winter is therefore an explanation for the higher variability during this season.

GWs can propagate both eastward and westward, but only against the zonal flow, implying the presence of eastward-propagating GWs during summer and westward-propagating GWs during winter. The extratropical meso- and stratospheric zonal winds are very weak and change direction during the equinoxes, resulting in a damping of both westward- and eastward-propagating GWs during these periods (Hoffmann et al., 2010). Enhanced PW activity is observed at the same time (Stray et al., 2014). Temperature enhancements after the spring equinox are related to the final breakdown of the polar vortex or the last stratospheric warming event (Shepherd et al., 2002). Several studies have observed a "springtime tongue" of westward flow between 85 and 100 km, occurring approximately from day 95 to 120, reflecting the final warming (e.g. Hoffmann et al., 2010; Manson et al., 2002). The final warming is characterised by forced planetary Rossby waves that exert a strong westward wave drag from the stratosphere up to 100 km.

Enhanced PW activity has also been observed during midsummer, due to interhemispheric propagation of PWs into the summer mesopause (Stray et al., 2014; Hibbins et al., 2009). Also, enhanced short-period GW activity has been observed during summer (Hoffmann et al., 2010). Increased temperatures during midsummer may thus be a result of the combined effect of upward-propagating GWs and interhemispheric propagation of PWs.

Several studies have identified large temperature amplitude perturbations during the autumn equinox in particular (Taylor et al., 2001; Liu et al., 2001). The same signature is hard to find in our data. Hoffmann et al. (2010) find latitudinal differences in the amplitude of the semidiurnal meridional tide during the autumn equinox, observing stronger tidal amplitudes at Juliusruh (55° N, 13° E) compared with Andenes (69° N, 16° E). Manson et al. (2009) also find longitudinal differences in tides at high latitudes. Reasons for not observing increased temperatures around the autumn equinox are not clear, and further investigations are needed in order to make conclusions.

The local temperature minimum in early winter is also seen in other temperature data from mid- and high latitudes (e.g. French and Burns, 2004; Holmen et al., 2013; Shepherd et al., 2004). French and Burns (2004) find a decrease in large-scale wave activity during midwinter which they associate with the observed temperature minimum, but identify this as a Southern Hemisphere phenomenon. Shepherd et al. (2004) attribute the decrease in temperature to early winter warming of the stratosphere, characterised by the growth of upward-propagating PWs from the troposphere which decelerate/reverses the eastward stratospheric jet, resulting in adiabatic heating of the stratosphere and adiabatic cooling of the mesosphere. However, Shepherd et al. used temperature data from 1991 to 1999, which is prior to the start of our temperature record, and timings of SSWs are different from year to year. We investigated the timing and occurrence of SSW events during the last decade using NASA reanalysis temperatures and zonal winds provided through the Modern-Era Retrospective analysis for Research and Applications (MERRA) project (NASA, 2016). Most SSWs occurring between 2003 and 2014 start in the beginning of January or mid-January. One exception is the major warming in 2003–2004, in which zonal winds started to decelerate in mid-December. There are signs of a minor warming in the transition between November and December 2012, but there is not enough evidence to conclude that the local minimum of NTMR temperatures starting in early November is associated with early winter warming of the stratosphere. It is more likely that the pronounced variability in temperatures we see in January and February (days $\sim$0–50) in Fig. 7 is a manifestation of the SSW effect.

5.2 Physical explanations for cooling and comparison with other studies

Other studies on long-term mesospheric temperature trends from mid and high latitudes yield mostly negative or near-zero trends. Few studies cover the same time period as ours, and few are from locations close to Tromsø. Hall et al. (2012) report a negative trend of $-4\,\mathrm{K} \pm 2\,\mathrm{K\,decade}^{-1}$ for temperatures derived from the meteor radar over Longyearbyen, Svalbard (78° N, 16° E) at 90 km height over the time period 2001 to 2011, while Holmen et al. (2014) find a near-zero trend for OH* airglow temperatures at $\sim$87 km height over Longyearbyen over the longer time period 1983 to 2013. Offermann et al. (2010) report a trend of $-2.3\,\mathrm{K} \pm 0.6\,\mathrm{K\,decade}^{-1}$ for $\sim$87 km height using OH* airglow measurements from Wuppertal (51° N, 7° E). It must be noted that the peak altitude of the OH* airglow layer can vary and thus affect the comparability of OH* airglow temperature trends and meteor radar temperature trends. Winick et al. (2009) report that the OH* airglow layer can range from 75 to $>$ 90 km, while the newer study by von Savigny (2015) indicates that the layer height at high latitudes is remarkably constant from 2003 to 2011. Beig (2011) report that most recent studies on mesopause region temperature trends show weak negative trends, which is in line with our results.

According to the formulation by Weatherhead et al. (1998), our time series is not long enough for significant trend detection. We need another $\sim$6 years of data before a

trend of magnitude $-2.2\,\mathrm{K} \pm 1.0\,\mathrm{K\,decade}^{-1}$ is significant. Response to solar variability has not been taken into account due to the length of the temperature record. Our slightly negative overall trend must therefore be considered tentative. The summer trend requires many more years of data before it can be considered significant, because is a near-zero trend. However, the winter trend can be considered detectable and also significantly different from zero, following the criteria from Weatherhead et al. (1998) and Tiao et al. (1990).

Our results indicate a cooling at 90 km altitude over Tromsø in winter. A general cooling of the middle atmosphere will cause a contraction of the atmospheric column, hence a lowering of upper-mesospheric pressure surfaces. The pressure model used as input to Eq. (2) is only seasonally dependent, so a possible trend in pressure at 90 km must be addressed. By looking at Eq. (2), it is evident that if pressure decreases, temperature will decrease even more. Incorporating a decreasing trend in the pressure model will then serve to further strengthen the negative temperature trend we observe.

It has been proposed that GWs may be a major cause of negative temperature trends in the mesosphere and thermosphere (Beig, 2011; Oliver et al., 2013). GWs effectively transport chemical species and heat in the region, and increased GW drag leads to a net effect of cooling above the turbopause (Yigit and Medvedev, 2009). GWs are shown to heat the atmosphere below about 110 km altitude, while they cool the atmosphere at higher altitudes by inducing a downward heat flux (Walterscheid, 1981). However, there are large regional differences regarding trends in GW activity. Hoffmann et al. (2011) find an increasing GW activity in the mesosphere in summer for selected locations, but Jacobi (2014) finds larger GW amplitudes during solar maximum and relates this to a stronger mesospheric jet during solar maximum, both for winter and summer. Since we have not conducted any gravity wave trend assessment in this study, we cannot conclude that GW activity is responsible for the negative temperature trend, but we cannot rule out its role either.

The stronger cooling trend for winter is also consistent with model studies. Schmidt et al. (2006) and Fomichev et al. (2007) show, using the HAMMONIA and CMAM models, respectively, that a doubling of the CO_2 concentration will lead to a general cooling of the middle atmosphere, but that the high-latitude summer mesopause will experience insignificant change or even slight warming. They propose that this is the result of both radiative and dynamical effects. In summer, the CO_2 radiative forcing is positive due to heat exchange between the cold polar mesopause and the warmer, underlying layers. Also, CO_2 doubling alters the mesospheric residual circulation. This change is caused by a warming in the tropical troposphere and cooling in the extratropical tropopause, leading to a stronger equator-to-pole temperature gradient and hence stronger midlatitude tropospheric westerlies. This causes the westerly gravity wave drag to weaken, resulting in decreased adiabatic cooling from a slower ascent of the upper-mesospheric circulation. However, it must be noted that our strong, negative NDJ trend may differ from a trend estimated for meteorological winter months.

5.3 Suitability of a meteor radar for estimation of neutral temperatures at 90 km height

As explained in Sect. 2, neutral air temperatures derived from meteor trail echoes depend on pressure, p, the zero-field reduced mobility of the ions in the trail, K_0, and ambipolar diffusion coefficients, D_a. K_0 will depend on the ion composition in the meteor trail, as well as the chemical composition of the atmosphere. The chemical composition of the atmosphere is assumed to not change significantly with season (Hocking, 2004). Unfortunately, the exact content of a meteor trail is unknown. Usually, a value for K_0 between 1.9×10^{-4} and $2.9 \times 10^{-4}\,\mathrm{m^2\,s^{-1}\,V^{-1}}$ is chosen, depending on what ion one assumes to be the main ion of the trail (Hocking et al., 1997). Even though we in this study have chosen a constant value for K_0 of $2.4 \times 10^{-4}\,\mathrm{m^2\,s^{-1}\,V^{-1}}$, some variability in K_0 is expected. According to Hocking (2004), variability can occur due to fragmentation of the incoming meteoroid, anisotropy in the diffusion rate, plasma instabilities and variations in the composition of the meteor trail. Using computer simulations, they report a typical variability in K_0 from meteor to meteor of 27 % and that the variability is most dominant at higher temperatures. Based on this, we cannot rule out sources of error due to the choice of K_0 as a constant, but since we have no possibility to analyse the composition of all meteor trails detected by the radar, we have no other choice than to choose a constant value for K_0.

How well ambipolar diffusion coefficients obtained for 90 km altitude are suited for calculating neutral temperatures has previously been widely discussed, e.g. by Hall et al. (2012) for the trend analysis of Svalbard meteor radar data, but will be shortly repeated here. For calculations of temperatures using meteor radar, ambipolar diffusion alone is assumed to determine the decay of the underdense echoes. Diffusivities are expected to increase exponentially with height through the region from which meteor echoes are obtained (Ballinger et al., 2008; Chilson et al., 1996). Hall et al. (2005) find that this is only the case between ~ 85 and ~ 95 km altitude, using diffusion coefficients delivered by NTMR from 2004. They find diffusivities less than expected above ~ 95 km and diffusivities higher than expected below ~ 85 km. Ballinger et al. (2008) obtain a similar result using meteor observations over northern Sweden. It has been proposed that processes other than ambipolar diffusion influence meteor decay times. If this is the case it may have consequences for the estimation of temperatures, and therefore it is important to investigate this further.

Departures of the anticipated exponential increase with height of molecular diffusion above ∼ 95 km in previous studies are attributed to the gradient-drift Farley–Buneman instability. The Farley–Buneman instability occurs where the trail density gradient and electric field are largest. Due to frequent collisions with neutral particles, electrons are magnetised while ions are left unmagnetised, causing electrons and ions to differ in velocity. Electrons then create an electric field perpendicular to the meteor trail, leading to anomalous fading times that can be an order of magnitude higher than those expected from ambipolar diffusion. The minimum altitude at which this occurs depends on the trail altitude, density gradient and latitude, and at high latitudes this altitude is ∼ 95 km. Therefore, using ambipolar diffusion rates to calculate trail altitudes above this minimum altitude may lead to errors of several kilometres, since the diffusion coefficients derived from the measurements are underestimated (Ballinger et al., 2008; Dyrud et al., 2001; Kovalev et al., 2008).

Reasons for the higher-than-expected diffusivities below ∼ 85 km are not completely understood, according to theory. Hall (2002) proposes that neutral turbulence may be responsible for overestimates of molecular diffusivity in the region ∼ 70–85 km, but this hypothesis is rejected by Hall et al. (2005) due to a lacking correlation between neutral air turbulent intensity and diffusion coefficients delivered by the NTMR radar. Other mechanisms for overestimates of molecular diffusivity include incorrect determination of echo altitude and fading times due to limitations of the radar (Hall et al., 2005).

Since the peak echo occurrence height is 90 km and this is also the height at which a minimum of disturbing effects occur, 90 km height is therefore considered the optimal height for temperature measurements using meteor radar. Ballinger et al. (2008) report that meteor radars in general deliver reliable daily temperature estimates near the mesopause using the method outlined in this study, but emphasise that one should exercise caution when assuming that observed meteor echo fading times are primarily governed by ambipolar diffusion. They propose, after Havnes and Sigernes (2005), that electron–ion recombination can impact meteor echo decay times. This can especially affect the weaker echoes, hence this effect can lead to an underestimation of temperatures.

Determination of temperatures from meteor radar echo times is a non-trivial task, mainly because the calculation of ambipolar diffusion coefficients depends on the ambient atmospheric pressure. By using radar echo decay times to calculate ambipolar diffusion coefficients from Eq. (1), we can get an estimate for T^2/p from Eq. (2). Input of pressure values into the equation will thus provide atmospheric temperatures. However, measurements of pressure are rare and difficult to achieve at 90 km height, and often one has to rely on model values. Traditionally, pressure values at 90 km have been calculated using the ideal gas law, taking total mass density from atmospheric models, e.g. the Mass Spectrometer and Incoherent Scatter Radar (MSIS) models, where the newest version is NRLMSISE-00. It is hard to verify the pressure values derived from the models because of lack of measurements to compare the model to; hence using the pressure values may result in uncertainties of estimated atmospheric temperatures. In this study, we obtained pressure values from measurements of mass densities obtained from falling spheres combined with sodium lidar from Andøya (69° N, 15.5° E) (Lübken, 1999; Lübken and von Zahn, 1991). All measurements have been combined to give a yearly climatology, that is, one pressure value for each day of the year. Since Andøya is located in close proximity to Tromsø (approximately 120 km), the pressure values are considered appropriate for our calculations of neutral temperatures. One disadvantage with using pressure values obtained from the falling sphere measurements is that no day-to-day variations are taken into account, only the average climatology.

6 Conclusions

A number of long-period oscillations ranging from ∼ 9 days to a year were found in the NTMR temperature data. Temperature variability observed may, to a large extent, be explained by the large-scale circulation of the middle atmosphere and the corresponding activity in waves propagating from below. Higher temperature variability in winter is due to the presence of upward-propagating PWs during this season, in contrast to summer, when easterly winds in the middle atmosphere are blocking vertical propagation of long-period PWs into the MLT region. The variability is particularly high in January and February, which are periods where SSW events occur frequently. In addition to the general maximum of temperatures in winter and minimum in summer, our data show a local temperature enhancement around day 210, a local minimum in early winter and reduction of the strong, negative seasonal gradient after the spring equinox. The reduction of the strong, negative seasonal gradient after the spring equinox is related to the final breakdown of the polar vortex (Shepherd et al., 2002), while the increase during summer is most likely associated with a combined effect of upward-propagating GWs and interhemispheric propagation of PWs (Stray et al., 2014; Hoffmann et al., 2010). No evident reason can be found for the local temperature minimum in early winter or the fact that we do not see enhanced temperatures during the autumn equinox, as identified by others (e.g. Taylor et al., 2001; Liu et al., 2001).

The trend for NTMR temperatures at 90 km height over Tromsø was found to be $-2.2\,\mathrm{K} \pm 1.0\,\mathrm{K\,decade^{-1}}$. Summer (May, June, July) and winter (November, December, January) trends are $-0.3\,\mathrm{K} \pm 3.1$ and $-11.6\,\mathrm{K} \pm 4.1\,\mathrm{K\,decade^{-1}}$, respectively. Following the criterion from Weatherhead et al. (1998), the temperature record is only long enough for the NDJ trend to be con-

sidered detectable. Response to solar variability was not incorporated in the trend, due to the time series being shorter than the corresponding solar cycle. However, when looking at the progression from high solar flux to solar minimum and back to solar maximum we see, to some extent, that there is a conjunction between low solar flux values and negative temperature fit residuals and vice versa.

A weak overall cooling trend is in line with other recent studies on mesopause region temperature trends. A cooling of the middle atmosphere will cause a lowering of upper-mesospheric pressure surfaces. By implementing a negative trend in pressure at 90 km into the equation that we use for estimating temperatures, the negative temperature trend is enhanced, which reinforces our finding of a cooling trend. The most accepted theory behind a cooling of the middle atmosphere is increased greenhouse gas emissions, which may lead to a change in dynamics. Our results yield a more negative trend in winter compared with summer, which may be explained by radiative and dynamical effects. In summer, a larger heat exchange takes place from atmospheric layers below the cold, polar mesopause. Weakening of gravity wave drag leads to weakening of the mesospheric residual circulation, which counteracts cooling. These effects occur due to increased CO_2 concentrations in the atmosphere, according to model studies.

7 Data availability

Meteor echo fading times from the NTMR radar used to calculate ambipolar diffusion coefficients and neutral temperatures are available upon request from Chris Hall at Tromsø Geophysical Observatory (chris.hall@uit.no). The Aura MLS temperature data are publicly available from the NASA Jet Propulsion Laboratory at http://mls.jpl.nasa.gov/index-eos-mls.php.

Acknowledgements. The research for this article was financially supported by The Research Council of Norway through contract 223252/F50 (CoE). NTMR operation was supported by Research Project KP-9 of National Institute of Polar Research. The authors are grateful to the NASA EOS Aura MLS team for providing free access to the MLS temperature data, and to Frank Mulligan at Maynooth University, Ireland, for providing downloaded data specific for Tromsø. In addition, the authors wish to express their appreciation to the referees of this paper.

Edited by: G. Stiller

References

Akmaev, R. A. and Fomichev, V. I.: Cooling of the mesosphere and lower thermosphere due to doubling of CO_2, Ann. Geophys., 16, 1501–1512, doi:10.1007/s00585-998-1501-z, 1998.

Akmaev, R. A. and Fomichev, V. I.: A model estimate of cooling in the mesosphere and lower thermosphere due to the CO_2 increase over the last 3–4 decades, Geophys. Res. Lett., 27, 2113–2116, doi:10.1029/1999GL011333, 2000.

Ballinger, A. P., Chilson, P. B., Palmer, R. D., and Mitchell, N. J.: On the validity of the ambipolar diffusion assumption in the polar mesopause region, Ann. Geophys., 26, 3439–3443, doi:10.5194/angeo-26-3439-2008, 2008.

Beig, G.: Long-term trends in the temperature of the mesosphere/lower thermosphere region: 1. Anthropogenic influences, J. Geophys. Res., 116, A00H11, doi:10.1029/2011JA016646, 2011.

Bittner, M., Offermann, D., and Graef, H. H.: Mesopause temperature variability above a midlatitude station in Europe, J. Geophys. Res., 105, 2045–2058, doi:10.1029/1999JD900307, 2000.

Cervera, M. A. and Reid, I. M.: Comparison of atmospheric parameters derived from meteor observations with CIRA, Radio Sci., 35, 833–843, doi:10.1029/1999RS002226, 2000.

Chilson, P. B., Czechowsky, P., and Schmidt, G.: A comparison of ambipolar diffusion coefficients in meteor trains using VHF radar and UV lidar, Geophys. Res. Lett., 23, 2745–2748, doi:10.1029/96gl02577, 1996.

Dyrland, M. E., Hall, C. M., Mulligan, F. J., Tsutsumi, M., and Sigernes, F.: Improved estimates for neutral air temperatures at 90 km and 78° N using satellite and meteor radar data, Radio Sci., 45, RS4006, doi:10.1029/2009rs004344, 2010.

Dyrud, L. P., Oppenheim, M. M., and vom Endt, A. F.: The anomalous diffusion of meteor trails, Geophys. Res. Lett., 28, 2775–2778, doi:10.1029/2000GL012749, 2001.

Espy, P. J. and Stegman, J.: Trends and variability of mesospheric temperature at high-latitudes, Phys. Chem. Earth., 27, 543–553, doi:10.1016/S1474-7065(02)00036-0, 2002.

Fomichev, V. I., Jonsson, A. I., de Grandpré, J., Beagley, S. R., McLandress, C., Semeniuk, K., and Shepherd, T. G.: Response of the middle atmosphere to CO_2 doubling: Results from the Canadian Middle Atmosphere Model, J. Climate, 20, 1121–1144, doi:10.1175/JCLI4030.1, 2007.

French, W. J. R. and Burns, G. B.: The influence of large-scale oscillations on long-term trend assessment in hydroxyl temperatures over Davis, Antarctica, J. Atmos. Sol.-Terr. Phys., 66, 493–506, doi:10.1016/j.jastp.2004.01.027, 2004.

French, W. J. R. and Klekociuk, A. R.: Long-term trends in Antarctic winter hydroxyl temperatures, J. Geophys. Res., 116, D00P09, doi:10.1029/2011JD015731, 2011.

French, W. J. R. and Mulligan, F. J.: Stability of temperatures from TIMED/SABER v1.07 (2002–2009) and Aura/MLS v2.2 (2004–2009) compared with OH(6–2) temperatures observed at Davis Station, Antarctica, Atmos. Chem. Phys., 10, 11439–11446, doi:10.5194/acp-10-11439-2010, 2010.

García-Comas, M., Funke, B., Gardini, A., López-Puertas, M., Jurado-Navarro, A., von Clarmann, T., Stiller, G., Kiefer, M., Boone, C. D., Leblanc, T., Marshall, B. T., Schwartz, M. J., and Sheese, P. E.: MIPAS temperature from the stratosphere to the lower thermosphere: Comparison of vM21 with ACE-FTS, MLS, OSIRIS, SABER, SOFIE and lidar measurements, At-

mos. Meas. Tech., 7, 3633–3651, doi:10.5194/amt-7-3633-2014, 2014.

Hall, C. M.: On the influence of neutral turbulence on ambipolar diffusivities deduced from meteor trail expansion, Ann. Geophys., 20, 1857–1862, doi:10.5194/angeo-20-1857-2002, 2002.

Hall, C. M., Aso, T., Tsutsumi, M., Nozawa, S., Manson, A. H., and Meek, C. E.: *Letter to the Editior* Testing the hypothesis of the influence of neutral turbulence on the deduction of ambipolar diffusivities from meteor trail expansion, Ann. Geophys., 23, 1071–1073, doi:10.5194/angeo-23-1071-2005, 2005.

Hall, C. M., Aso, T., Tsutsumi, M., Höffner, J., Sigernes, F., and Holdsworth, D. A.: Neutral air temperatures at 90 km and 70° N and 78° N, J. Geophys. Res., 11, D14105, doi:10.1029/2005JD006794, 2006.

Hall, C. M., Dyrland, M. E., Tsutsumi, M., and Mulligan, F. J.: Temperature trends at 90 km over Svalbard, Norway (78° N 16° E), seen in one decade of meteor radar observations, J. Geophys. Res.-Atmos., 117, D08104, doi:10.1029/2011JD017028, 2012.

Havnes, O. and Sigernes, F.: On the influence of background dust on radar scattering from meteor trails, J. Atmos. Sol.-Terr. Phys., 67, 659–664, doi:10.1016/j.jastp.2004.12.009, 2005.

Hibbins, R. E., Jarvis, M. J., and K Ford, E. A.: Quasi-biennial oscillation influence on long-period planetary waves in the Antarctic upper mesosphere, J. Geophys. Res., 114, D09109, doi:10.1029/2008JD011174, 2009.

Hocking, W. K.: Temperatures using radar-meteor decay times, Geophys. Res. Lett., 26, 3297–3300, doi:10.1029/1999GL003618, 1999.

Hocking, W. K.: Radar meteor decay rate variability and atmospheric consequences, Ann. Geophys., 22, 3805–3814, doi:10.5194/angeo-22-3805-2004, 2004.

Hocking, W. K., Thayaparan, T., and Jones, J.: Meteor decay times and their use in determining a diagnostic mesospheric temperature-pressure parameter: methodology and one year of data, Geophys. Res. Lett., 24, 2977–2980, doi:10.1029/97gl03048, 1997.

Hoffmann, P., Becker, E., Singer, W., and Placke, M.: Seasonal variation of mesospheric waves at northern middle and high latitudes, J. Atmos. Sol.-Terr. Phys., 72, 1068–1079, doi:10.1016/j.jastp.2010.07.002, 2010.

Hoffmann, P., Rapp, M., Singer, W., and Keuer, D.: Trends of mesospheric gravity waves at northern middle latitudes during summer, J. Geophys. Res., 116, D00P08, doi:10.1029/2011JD015717, 2011.

Holdsworth, D. A., Morris, R. J., Murphy, D. J., Reid, I. M., Burns, G. B., and French, W. J. R.: Antarctic mesospheric temperature estimation using the Davis mesosphere-stratosphere-troposphere radar, J. Geophys. Res.-Atmos., 111, D05108, doi:10.1029/2005jd006589, 2006.

Holmen, S. E., Dyrland, M. E., and Sigernes, F.: Mesospheric temperatures derived from three decades of hydroxyl airglow measurements from Longyearbyen, Svalbard (78° N), Acta Geophys., 62, 302–315, doi:10.2478/s11600-013-0159-4, 2013.

Holmen, S. E., Dyrland, M. E., and Sigernes, F.: Long-term trends and the effect of solar cycle variations on mesospheric winter temperatures over Longyearbyen, Svalbard (78° N), J. Geophys. Res.-Atmos., 119, 6596–6608, doi:10.1002/2013jd021195, 2014.

Horne, J. H. and Baliunas, S. J.: A prescription for period analysis for unevenly sampled time series, Astrophys. J., 302, 757–763, doi:10.1086/164037, 1986.

Jacobi, C.: Long-term trends and decadal variability of upper mesosphere/lower thermosphere gravity waves at midlatitudes, J. Atmos. Sol.-Terr. Phys., 118, 90–95, doi:10.1016/j.jastp.2013.05.009, 2014.

Kovalev, D. V., Smirnov, A. P., and Dimant, Y. S.: Modeling of the Farley-Buneman instability in the E-region ionosphere: a new hybrid approach, Ann. Geophys., 26, 2853–2870, doi:10.5194/angeo-26-2853-2008, 2008.

Laštovicka, J., Akmaev, R. A., Beig, G., Bremer, J., Emmert, J. T., Jacobi, C., Jarvis, M. J., Nedoluha, G., Portnyagin, Yu. I., and Ulich, T.: Emerging pattern of global change in the upper atmosphere and ionosphere, Ann. Geophys., 26, 1255–1268, doi:10.5194/angeo-26-1255-2008, 2008.

Laštovička, J., Solomon, S. C., and Qian, L.: Trends in the neutral and ionized upper atmosphere, Space Sci. Rev., 168, 113–145, doi:10.1007/s11214-011-9799-3, 2012.

Liu, H.-L., Roble, R. G., Taylor, M. J., Pendleton Jr., W. R.: Mesospheric planetary waves at northern hemisphere fall equinox, Geophys. Res. Lett., 28, 1903–1906, doi:10.1029/2000GL012689, 2001.

Lübken, F.-J.: Thermal structure of the Arctic summer mesosphere, J. Geophys. Res.-Atmos., 104, 9135–9149, doi:10.1029/1999JD900076, 1999.

Lübken, F.-J. and von Zahn, U.: Thermal structure of the mesopause region at polar latitudes, J. Geophys. Res.-Atmos., 96, 20841–20857, doi:10.1029/91JD02018, 1991.

Lübken, F.-J., Berger, U., and Baumgarten, G.: Temperature trends in the midlatitude summer mesopause, J. Geophys. Res.-Atmos., 118, 13347–13360, doi:10.1002/2013JD020576, 2013.

Manabe, S. and Wetherald, R. T.: The effects of doubling the CO_2 concentration on the climate of a general circulation model, J. Atmos. Sci., 32, 3–15, doi:10.1175/1520-0469(1975)032<0003:TEODTC>2.0.CO;2, 1975.

Manson, A. H., Meek, C. E., Stegman, J., Espy, P. J., Roble, R. G., Hall, C. M., Hoffmann, P., and Jacobi, Ch.: Springtime transitions in mesopause airglow and dynamics: photometer and MF radar observations in the Scandinavian and Canadian sectors, J. Atmos. Sol.-Terr. Phys., 64, 1131–1146, doi:10.1016/S1364-6826(02)00064-0, 2002.

McKinley, D. W. R.: Meteor Science and Engineering, McGraw-Hill, New York, 1961.

NASA: Annual Meteorological Statistics, National Aeronautics Space Administration, available at: http://acdb-ext.gsfc.nasa.gov/Data_services/met/ann_data.html, last access: April 2016.

NASA Jet Propulsion Laboratory: EOS Microwave Limb Sounder, available at: http://mls.jpl.nasa.gov/index-eos-mls.php, last access: January 2015.

Niciejewski, R. J. and Killeen, T. L.: Annual and semi-annual temperature oscillations in the upper mesosphere, Geophys. Res. Lett., 22, 3243–3246, doi:10.1029/95GL02411, 1995.

Offermann, D., Hoffmann, P., Knieling, P., Koppmann, R., Oberheide, J., and Steinbrecht, W.: Long-term trends and solar cycle variations of mesospheric temperatures and dynamics, J. Geophys. Res., 115, D18127, doi:10.1029/2009JD013363, 2010.

Ogawa, Y., Motoba, T., Buchert, S. C., Häggström, I., and Nozawa, S.: Upper atmosphere cooling over the past 33 years, Geophys. Res. Lett., 41, 5629–5635, doi:10.1002/2014GL060591, 2014.

Oliver, W. L., Zhang, S.-R., and Goncharenko, L. P.: Is thermospheric global cooling caused by gravity waves?, J. Geophys. Res., 118, 3898–3908, doi:10.1002/jgra.50370, 2013.

Press, W. H. and Rybicki, G. B.: Fast algorithm for spectral analysis of unevenly sampled data, Astrophys. J. Part 1, 338, 277–280, doi:10.1086/167197, 1989.

Rees, D., Rishbeth, H., and Kaiser, T. R.: Winds and temperatures in the auroral zone and their relations to geomagnetic activity, Philos. T. R. Soc. A, 271, 563–575, doi:10.1098/rsta.1972.0024, 1972.

Roble, R. G. and Dickinson, R. E.: How will changes in carbon dioxide and methane modify the mean structure of the mesosphere and thermosphere?, Geophys. Res. Lett., 16, 1441–1444, doi:10.1029/GL016i012p01441, 1989.

Salby, M. L.: Rossby normal modes in nonuniform background configurations. Part I: Simple fields, J. Atmos. Sci., 38, 1803–1826, doi:10.1175/1520-0469(1981)038<1803:RNMINB>2.0.CO;2, 1981a.

Salby, M. L.: Rossby normal modes in nonuniform background configurations. Part II: Equinox and solstice conditions, J. Atmos. Sci., 38, 1827–1840, doi:10.1175/1520-0469(1981)038<1827:RNMINB>2.0.CO;2, 1981b.

Scargle, J. D.: Studies in astronomical time series analysis. II. Statistical aspects of spectral analysis of unevenly spaced data, Astrophys. J., 263, 835–853, doi:10.1086/160554, 1982.

Schmidt, H., Brasseur, G. P., Charron, M., Manzini, E., Giorgetta, M. A., and Diehl, T.: The HAMMONIA Chemistry Climate Model: Sensitivity of the mesopause region to the 11-year solar cycle and CO_2 doubling, J. Climate, 19, 3903–3931, doi:10.1175/JCLI3829.1, 2006.

Shepherd, M. G., Espy, P. J., She, C. Y., Hocking, W., Keckhut, P., Gavrilyeva, G., Shepherd, G. G., and Naujokat, B.: Springtime transition in upper mesospheric temperature in the northern hemisphere, J. Atmos. Sol.-Terr. Phys., 64, 1183–1199, doi:10.1016/S1364-6826(02)00068-8, 2002.

Shepherd, M. G., Rochon, Y. J., Offermann, D., Donner, M., and Espy, P. J.: Longitudinal variability of mesospheric temperatures during equinox at middle and high latitudes, J. Atmos. Sol.-Terr. Phys., 66, 463–479, doi:10.1016/j.jastp.2004.01.036, 2004.

Stray, N. H., de Wit, R. J., Espy, P. J., and Hibbins, R. E.: Observational evidence for temporary planetary wave forcing of the MLT during fall equinox, Geophys. Res. Lett., 41, 6281–6288, doi:10.1002/2014GL061119, 2014.

Taylor, M. J., Pendleton Jr., W. R., Liu, H.-L., She, C. Y., Gardner, L. C., Roble, R. G., and Vasoli, V.: Large amplitude pertubations in mesospheric OH Meinel and 87-km Na lidar temperatures around the autumnal equinox, Geophys. Res. Lett., 28, 1899–1902, doi:10.1029/2000GL012682, 2001.

Tiao, G. C., Reinsel, G. C., Xu, D., Pedrick, J. H., Zhu, X., Miller, A. J., DeLuisi, J. J., Mateer, C. L., and Wuebbles, D. J.: Effects of autocorrelation and temporal sampling schemes on estimates of trend and spatial correlation, J. Geophys. Res.-Atmos., 95, 20507–20517, doi:10.1029/JD095iD12p20507, 1990.

von Savigny, C.: Variability of OH(3-1) emission altitude from 2003 to 2011: Long-term stability and universality of the emission rate-altitude relationship, J. Atmos. Sol.-Terr. Phys., 127, 120–128, doi:10.1016/j.jastp.2015.02.001, 2015.

Walterscheid, R. L.: Dynamical cooling induced by dissipating internal gravity waves, Geophys. Res. Lett., 8, 1235–1238, doi:10.1029/GL008i012p01235, 1981.

Weatherhead, E. C., Reinsel, G. C., Tiao, G. C., Meng, X.-L., Choi, D., Cheang, W.-K., Keller, T., DeLuisi, J., Wuebbles, D. J., Kerr, J. B., Miller, A. J., Oltmans, S. J., and Frederick, J. E.: Factors affecting the detection of trends: Statistical considerations and applications to environmental data, J. Geophys. Res., 103, 17149–17161, doi:10.1029/98JD00995, 1998.

Winick, J. R., Wintersteiner, P. P., Picard, R. H., Esplin, D., Mlynczak, M. G., Russell III, J. M., and Gordley, L. L.: OH layer characteristics during unusual boreal winters of 2004 and 2006, J. Geophys. Res., 114, A02303, doi:10.1029/2008JA013688, 2009.

Yigit, E. and Medvedev, A. S.: Heating and cooling of the thermosphere by internal gravity waves, Geophys. Res. Lett., 36, L14807, doi:10.1029/2009GL038507, 2009.